

# High-Performance Multiband THz MIMO Antenna for Future 6G Wireless Communications with Machine Learning Validation

Md. Ashraful Haque<sup>1</sup>, Md. Sharif Ahammed<sup>1</sup>, Jamal Hossain Nirob<sup>1</sup>, Jun-Jiat Tiang<sup>2,\*</sup>,  
and Narinderjit Singh Sawaran Singh<sup>3</sup>

<sup>1</sup> Department of Electrical and Electronic Engineering, Daffodil International University, Dhaka, 1207 Bangladesh

<sup>2</sup> Centre for Wireless Technology, CoE for Intelligent Network, Faculty of Artificial Intelligence and Engineering, Multimedia University, Persiaran Multimedia, 63100 Cyberjaya, Selangor, Malaysia

<sup>3</sup> Faculty of Data Science and Information Technology, INTI International University, Persiaran Perdana BBN, Putra Nilai, Nilai 71800, Negeri Sembilan, Malaysia

Email: limon.ashraf@gmail.com (M.A.H.); sharif33-1152@diu.edu.bd (M.S.A.); jamal33-1243@diu.edu.bd (J.H.N.),  
jjtiang@mmu.edu.my (J.J.T.); narinderjits.sawaran@newinti.edu.my (N.S.S.S.)

\*Corresponding Author

**Abstract**—This study presents a comprehensive industrial and innovation design along with an in-depth analysis of a THz Multiple Input Multiple Output (MIMO) antenna intended for future 6G communication systems. The antenna utilizes polyimide as the substrate and graphene as the patch material, with copper serving as the ground plane. This design enables the antenna to operate across six distinct frequency bands, making it a multiband antenna. The resonance frequencies of the antenna are 3.512 THz, 4.4448 THz, 6.704 THz, 7.672 THz, 8.664 THz, and 9.672 THz, with corresponding gains of 11.72 dB, 12.59 dB, 13.077 dB, 13.945 dB, 14.77 dB, and 16.028 dB, respectively. To further understand the electrical behavior of the antenna, an RLC equivalent circuit was developed using Advanced Design System (ADS) software. Subsequently, we employed supervised regression Machine Learning techniques following extensive data sampling using CST MWS (Microwave Studio) simulations. The results, highlighted by robust R-squared and variance scores, demonstrate that Extra Trees Regression delivers exceptional accuracy, approaching 98%. Additionally, it achieves the lowest error in predicting resonance frequency.

**Keywords**—industrial and innovation, THz antenna, Multiple-Input Multiple-Output (MIMO), Graphene, Sixth-Generation (6G), Envelop Correlation Coefficient (ECC), Radio Link Control (RLC)

## I. INTRODUCTION

The demand for ultra-fast, highly reliable, and massively connected wireless networks is accelerating with the evolution toward Sixth-Generation (6G) communication systems [1]. As the limitations of existing Gigahertz (GHz)-based technologies become more pronounced—particularly in terms of bandwidth scarcity,

latency, and spectral congestion—the focus of research is rapidly shifting toward the Terahertz (THz) frequency spectrum. Spanning from 0.1 to 10 THz, this underutilized spectral region holds immense potential to meet the extreme data rate and low-latency requirements of future applications [2]. THz communication offers transformative capabilities for next-generation use cases such as real-time Virtual Reality (VR), wireless holographic imaging, high-speed backhaul networks, and ultra-reliable connectivity for dense Internet of Things (IoT) deployments [3]. However, exploiting this frequency range introduces significant design challenges, especially in antenna development. Conventional antenna materials and architectures often fall short in achieving the required performance due to increased propagation losses, miniaturization difficulties, and limited tunability at THz frequencies [4].

Among emerging solutions, graphene has attracted substantial attention as a groundbreaking material for THz antenna systems. Its extraordinary electrical conductivity, high carrier mobility, and ability to support surface plasmon polaritons make it exceptionally well-suited for miniaturized, high-performance THz components [5]. Graphene-based antennas offer reconfigurability and integration capabilities that are difficult to achieve with traditional metallic designs, paving the way for compact and efficient THz systems [6]. Despite these promising developments, current THz antenna designs still face trade-offs between gain, bandwidth, efficiency, and mutual coupling—particularly in multi-element configurations required for 6G MIMO systems [7]. To bridge this gap, the present work introduces a novel graphene-based antenna optimized for THz operation. The proposed design aims to deliver wide bandwidth, high gain, superior isolation, and excellent diversity performance, indicating potential suitability for integration into future 6G wireless networks. In recent years, the field of

Manuscript received June 19, 2025; revised August 19, 2025; accepted August 27, 2025; published February 12, 2026.

Terahertz (THz) technology has experienced significant advancements, particularly in the development of high-performance Multiple Input Multiple Output (MIMO) antennas for various applications such as high-speed wireless communications, imaging, and sensing [8]. The THz frequency band, typically spanning from 0.1 to 10 THz, holds immense promise for ultra-high-speed data transfer and high-resolution imaging due to its high frequency and a wide available bandwidth. Nevertheless, the design of antennas that can efficiently operate within this range presents numerous challenges, including the achievement of wide bandwidth, high gain, and low return loss.

The existing literature on THz MIMO antenna designs reveals various advancements and limitations across multiple performance metrics. In Ref. [9], a dual-port antenna operating at 3.5 THz achieves high isolation of 55 dB and moderate gain of 7.23 dB with a bandwidth of 0.6 THz. Khaleel *et al.* [10] demonstrated a bandwidth of only 0.3 THz with gain values between 4.5 and 10 dB and good isolation of 54 dB. The antenna in Ref. [11] operates at 2.8 THz with a bandwidth of 1 THz and efficiency of 98%, but its isolation is limited to 23 dB and ECC is relatively high at 0.004859. Ibrahim and Gaber [12] presented a two-port antenna operating at a resonance frequency of 3.32 THz with a bandwidth of 1.25 THz. Although it achieves a moderate gain of 10.8 dB, the relatively low isolation of 20 dB limits its effectiveness for robust MIMO performance. Amraoui *et al.* [13] featured a four-port antenna resonating at two distinct frequencies, 0.445 THz and 0.540 THz, and achieves an efficiency exceeding 81%.

However, it suffers from relatively low gain values of 7.9 dB and 6.6 dB, along with weak isolation of only  $-20$  dB, which significantly limits its suitability for performance-critical MIMO applications. In Ref. [14], the antenna works at 2.2 THz with a bandwidth of 0.78 THz and efficiency of 96%, yet the gain is limited to 4.4 dB and isolation remains low at 20 dB. Babu *et al.* [15] provided modest performance with a 0.4 THz bandwidth and gain of 5.49 dB, achieving 85.24% efficiency but limited isolation of 25 dB and a relatively high ECC of 0.015. The design presented in Ref. [16] operates at dual resonance frequencies of 0.395 THz and 0.629 THz, achieving bandwidths of 0.0095 THz and 0.024 THz, respectively. Although it reaches a peak efficiency of 92.48%, the narrow bandwidths of 0.0095 and 0.024 THz and moderate gain values of 3.89 dB and 5.17 dB limit its applicability in wideband THz communication systems.

The proposed antenna overcomes these challenges by achieving multi-band operation at 3.5, 4.44, 6.7, 7.67, 8.66, and 9.67 THz with wide bandwidths ranging from 0.8 to 1 THz. It maintains excellent isolation performance, ranging from 38 dB to 85 dB, and provides significantly higher gain values up to 16.03 dB. The antenna also ensures superior radiation efficiency, ranging from 89.5% to 98.35%, and excellent diversity performance with an exceptionally low ECC of 0.0001 and a DG of 9.99948. Moreover, the integration of both machine learning techniques and RLC circuit modeling further enhances the antenna's novelty and design accuracy, enabling it to address the primary limitations found in the existing works, as detailed in Table I.

TABLE I. RESULT COMPARISON BETWEEN THE PROPOSED MIMO ANTENNA AND OTHER PUBLICATIONS.

Parameter	[9]	[10]	[11]	[12]	[13]	[14]	[15]	[16]	Proposed
Resonance Frequency (THz)	3.5	1.9	2.8	3.32	0.445, 0.540	2.2	0.35–0.75	0.395, 0.629	3.5, 4.44, 6.7, 7.67, 8.66, 9.67
Bandwidth (THz)	0.6	0.3	1	1.25	N/A	0.78	0.4	0.0095, 0.024	0.9, 0.8, 0.98, 0.93, 0.92, 1
Port	2	2	2	2	4	2	2	4	2
Isolation	55	54	23	$-20$	$-20$	20	25	$-20$	38, 54, 70, 72, 84, 85
Gain (dB)	7.23	4.5–10	N/A	10.8	7.9, 6.6	4.4	5.49	3.89, 5.17	11.7, 12.6, 13.07, 13.94, 14.77, 16.03
Efficiency (%)	N/A	N/A	98	80	81.39, 83.36	96	85.24	82, 92.48	89.5, 98.35, 97.9, 93, 91.22, 91.9
ECC & DG (dB)	0.000168 & 9.999	0.000023 & 9.99	0.004859 & 9.99	0.005 & 10	0.0001 & 10	0.006 & 9.9998	0.015 & 9.99	0.0125, 10	0.0001 & 9.999
ML/RLC	No/ No	No/ No	No/ No	No/ No	Yes/Yes	No/ No	No/ No	No/Yes	Yes/Yes
Substrate Material	N/A	N/A	Teflon	SiO <sub>2</sub>	Polyimide	Polyimide	Polyimide	Polyimide	Polyimide

## II. RESEARCH GAP AND CONTRIBUTION

Although various graphene/polyimide-based THz MIMO antennas have been reported in recent literature, most designs primarily emphasize geometric modifications and full-wave electromagnetic simulations.

These approaches often overlook intelligent performance prediction and lack deeper physical validation methods. A significant gap identified in the

existing works is the absence of Machine Learning (ML)-based performance modeling. None of the studies listed in Table I incorporate ML algorithms to estimate key antenna parameters. The present work addresses this gap by integrating advanced supervised regression models to enable accurate prediction of antenna characteristics, facilitating faster and more efficient design optimization.

Another limitation in the reviewed literature is the lack of equivalent circuit validation. The proposed antenna design includes a detailed RLC circuit model, offering an

electrical representation that aligns closely with full-wave CST simulation results. This dual-layer validation approach enhances the credibility of the design, especially under constraints where experimental verification at THz frequencies is not feasible.

Key contributions of this work are summarized as follows:

- A high-performance multiband THz MIMO antenna featuring wide bandwidth, high gain, and strong isolation suitable for 6G wireless applications.
- The machine learning evaluation of regression techniques is substantially faster than a physical simulation model’s numerical solution, making them useful for process optimization. Regression models can also help isolate each design element’s role in reaching the intended results. The simulation’s predictions and outcomes showed close agreement.
- The results obtained from the developed RLC equivalent circuit were in excellent agreement with those obtained from the simulation.

These contributions collectively address critical shortcomings in current THz antenna research and offer a more comprehensive design and validation framework for next-generation communication systems.

### III. DESIGNING OF THE SINGLE-ELEMENT ANTENNA AND ITS RESULT

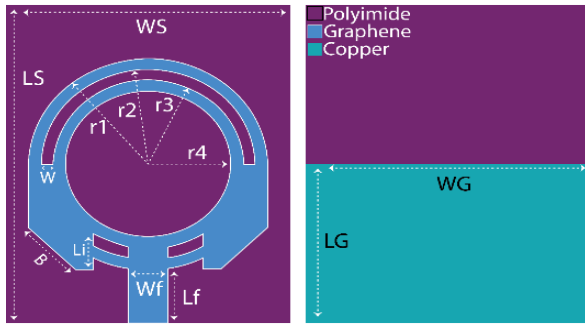


Fig. 1. Front and back side of single-element: (a) Front, (b) Back.

In Fig. 1, the single-element antenna incorporates four defined radius ( $r_1$ ,  $r_2$ ,  $r_3$ , and  $r_4$ ) that shape the arc segments, along with a strip Width ( $W$ ) and an arc gap ( $B$ ) for impedance control. At the bottom of the patch, a feed line of width ( $W_f$ ) and length ( $L_f$ ) connects to the radiating structure, while two small rectangular slots and spacing ( $L_i$ ) aid in tuning the antenna’s resonant characteristics. The back view displays a partial copper ground plane of Width ( $W_G$ ) and Length ( $L_G$ ), with the remaining surface left as exposed polyimide. This partial ground configuration, together with the arc-ring patch geometry, supports wideband or multi-band operation, making the design suitable for advanced high-frequency applications such as terahertz communications. In our single-element antenna, we have identified five resonance frequencies, which are 5.52 THz, 6.4 THz, 7.4 THz, 8.4 THz, and 9.4 THz. The return loss values corresponding to these frequencies are 49, 25, 32, 35, and 37, respectively. The achieved bandwidths were 0.75 THz (5.24–5.99 THz), 0.75 THz

(6.20–6.95 THz), 0.8 THz (7.10–7.90 THz), 0.8 THz (8.17–8.97 THz), and 0.86 THz (9.11–9.97 THz), corresponding to their respective resonant frequencies.

The gain of an antenna is a crucial parameter, and in the case of our antenna, it falls within the range of 9 to 14.6 dB. Additionally, the antenna’s efficiency ranges from 92% to 97%. The S11 and gain & efficiency are shown in Fig. 2 and Fig. 3, respectively. Table II provides a summary of the optimum parameters and dimensions for an antenna.

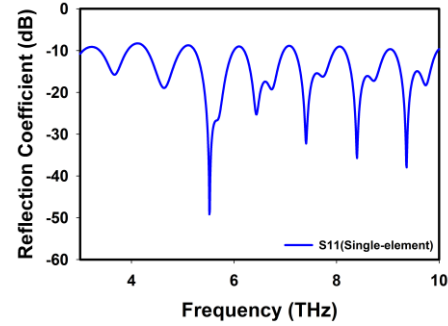


Fig. 2. S11 of the proposed single-element antenna.

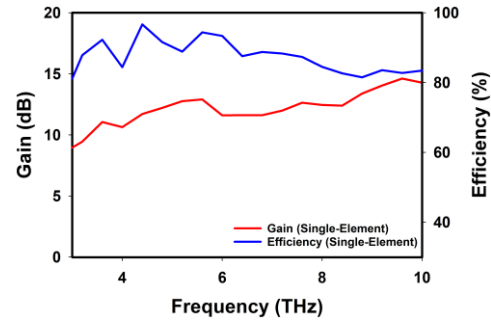


Fig. 3. Gain and efficiency of the proposed single-element antenna.

TABLE II. DESIGN PARAMETERS FOR THE ANTENNA

Parameter Name	Parameter Size (um)	Parameter name	Parameter Size (um)
Substrate Length (Ls)	150 $\mu\text{m}$	Inset Length (Li)	25 $\mu\text{m}$
Substrate Width (Ws)	120 $\mu\text{m}$	Radius 1 (r1)	50 $\mu\text{m}$
Patch Width (Wp)	100 $\mu\text{m}$	Radius 2 (r2)	45 $\mu\text{m}$
Patch Length (Lp)	100 $\mu\text{m}$	Radius 3 (r3)	40 $\mu\text{m}$
Ground Length (Lg)	75 $\mu\text{m}$	Radius 4 (r4)	35 $\mu\text{m}$
Ground Width (Wg)	75 $\mu\text{m}$	Gap Width (W)	5 $\mu\text{m}$
Feed Width (Wf)	16 $\mu\text{m}$	Patch cut (B)	20 $\mu\text{m}$
Feed Length (Lf)	50 $\mu\text{m}$		

### IV. EVOLUTION OF THE SINGLE ELEMENT ANTENNA

The evolution of the single-element antenna design unfolded through a meticulous process of iterative refinement across three distinct stages, each stage representing a significant milestone in the journey toward optimal performance. Fig. 4 and Fig. 5 present the structural progression and performance evolution of the proposed terahertz antenna design, respectively. Step 1 used a square patch fed by a microstrip line, but the absence of any resonance indicated poor impedance

matching, necessitating a design modification to excite resonant modes. In Step 2, the square patch was replaced with a semi-circular geometry, which altered the surface current distribution and slightly improved the return loss. However, the improvement was insufficient, prompting further changes. Consequently, Step 3 introduced a circular slot into the patch, effectively increasing the electrical path length and generating multiple resonances at 4.16 THz, 6.67 THz, 8.1 THz, and 8.56 THz. Despite this progress, the narrow bandwidth at each resonance prompted another round of design optimization. Step 4 added a concentric partial ring slot, enhancing coupling and multi-resonance behavior, but the bandwidth still fell short, leading to a final enhancement. The final step embedded additional inner slots within the patch to optimize electromagnetic coupling and minimize reflection across the operating range. This modification yielded five distinct resonances at 5.52 THz, 6.4 THz, 7.4 THz, 8.4 THz, and 9.4 THz, with corresponding return losses of 49 dB, 25 dB, 32 dB, 35 dB, and 37 dB. The respective bandwidths achieved were 0.75 THz, 0.75 THz, 0.8 THz, 0.8 THz, and 0.86 THz at their corresponding resonances. This systematic, step-by-step geometric evolution demonstrates how targeted structural modifications transform a simple patch into a high-performance, wideband terahertz antenna capable of supporting multiple well-matched resonances for advanced THz applications.

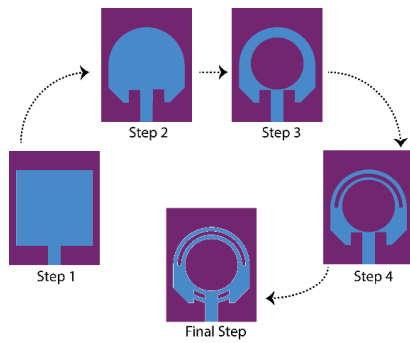


Fig. 4. Evaluation of single element antenna.

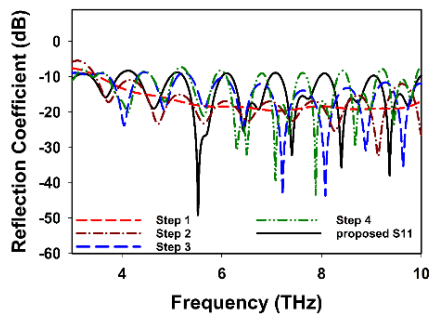


Fig. 5. Reflection coefficient at each design step of the single-element antenna.

## V. PARAMETRIC ANALYSIS

### A. Varying the Parameter of the Substrate LENGTH ( $L_s$ )

The influence of substrate length variation on the antenna reflection coefficient was examined for lengths of

145  $\mu\text{m}$  and 155  $\mu\text{m}$  (Fig. 6). The proposed configuration achieves the most profound resonance ( $-50$  dB) at approximately 6.0 THz, along with consistent multi-band behavior. Reducing the substrate length to 145  $\mu\text{m}$  slightly shifts specific resonances toward higher frequencies and produces a substantial dip near 9.5 THz, while the overall matching at intermediate bands is reduced. Increasing the substrate length to 155  $\mu\text{m}$  shifts resonances marginally toward lower frequencies and enhances some higher-frequency dips but increases ripple across the spectrum.

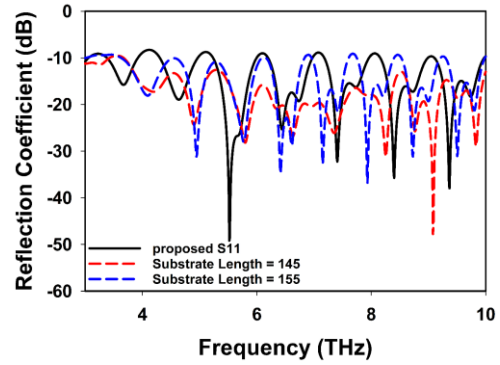


Fig. 6. Reflection coefficient for different substrate lengths.

### B. Changing the Parameter Named as Feed Width ( $W_f$ )

The effect of feed width variation on the antenna reflection coefficient was investigated over the 3–10 THz range, as shown in Fig. 7. Three cases were analyzed: the proposed feed width, 14  $\mu\text{m}$ , and 18  $\mu\text{m}$ . The proposed configuration exhibits the most profound resonance ( $-50$  dB) near 6.0 THz, along with multiple well-defined dips across the higher frequency bands, indicating superior impedance matching and stable multi-band operation. Reducing the feed width to 14  $\mu\text{m}$  shifts the lower resonances toward lower frequencies (4–4.5 THz) while reducing matching quality at higher bands. Increasing the feed width to 18  $\mu\text{m}$  shifts resonances slightly upward and enhances inevitable higher-frequency dips, but introduces stronger ripple across the spectrum. These results confirm that the proposed feed width offers the best trade-off between wideband performance and deep resonance characteristics.

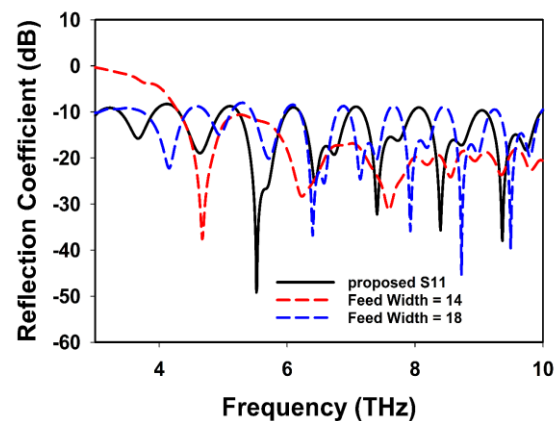


Fig. 7. Reflection coefficient for different feed lengths.

## VI. DESIGN OF THE PROPOSED ANTENNA AND ITS RESULT ANALYSIS

In Fig. 8, we can see the illustration of the proposed MIMO (Multiple-Input Multiple-Output) antenna. The antenna is developed by extending a single-element antenna design to achieve enhanced performance through careful decoupling techniques. The antenna employs graphene as the patch material. The design incorporates a decoupling structure made of graphene with a decoupling Length (LD) of 70  $\mu\text{m}$ , effectively minimizing mutual coupling between the antenna elements. The two patches are positioned at a separation Distance (DP) of 50  $\mu\text{m}$  to ensure adequate isolation while maintaining a compact layout. The substrate dimensions are optimized to 150  $\mu\text{m}$  in length ( $L_s$ ) and 250  $\mu\text{m}$  in width ( $W_s$ ).

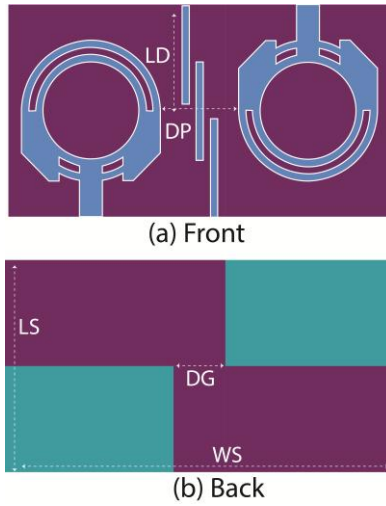


Fig. 8. The front and back sides of the proposed MIMO antenna.

### A. Reflection Coefficient and Transmission Coefficient

In Fig. 9, The designed THz MIMO antenna exhibits six distinct resonance frequencies at 3.5, 4.44, 6.7, 7.67, 8.66, and 9.67 THz. These frequencies are well-distributed across the THz spectrum, providing flexibility for various applications. The corresponding bandwidths are 0.9, 0.8, 0.98, 0.93, 0.92, and 1 THz, covering frequency ranges of 3–3.9, 4.1–4.9, 6.02–7, 7.01–7.94, 8.04–8.96, and 9–10 THz. The wide bandwidths ensure the antenna can handle high data rates and multiple communication channels, which is crucial for high-speed THz applications [17].

The return loss values at the six resonance frequencies are 49, 26, 37, 35, 40.89, and 85 dB. These values indicate excellent impedance matching across the operating frequencies, minimizing signal reflection and maximizing power transfer [18]. High return loss is indicative of the antenna's ability to efficiently transmit and receive signals without significant losses due to impedance mismatch [19].

Isolation between the ports of the MIMO antenna is a critical parameter to minimize mutual coupling and interference [20]. The isolation values at the resonance frequencies are 38, 54, 70, 72, 84, and 85dB. These high isolation values demonstrate the antenna's ability to operate effectively in a MIMO configuration, ensuring that the signals from different ports do not interfere with each

other, which is essential for maintaining signal integrity and improving system performance [21].

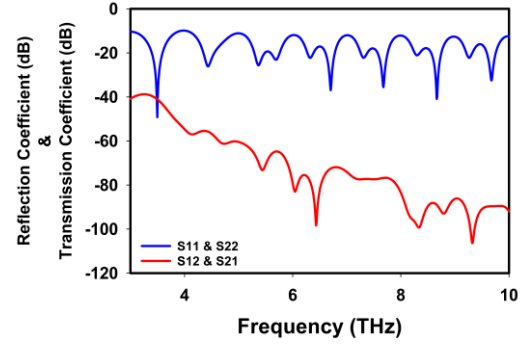


Fig. 9. S11 curve and return loss of the proposed MIMO antenna.

### B. Gain and Efficiency

The gain values for the antenna are 11.7, 12.6, 13.07, 13.94, 14.77, and 16.03 dB at the respective resonance frequencies shown in Fig. 10. These values indicate that the antenna can effectively amplify the transmitted and received signals, which is crucial for long-range communication and high-resolution imaging. The efficiency values are 89.5%, 98.35%, 97.9%, 93%, 91.22%, and 91.9%, showcasing the antenna's capability to convert input power into radiated power effectively [22]. High efficiency is particularly important in THz applications where signal attenuation can be significant [23].

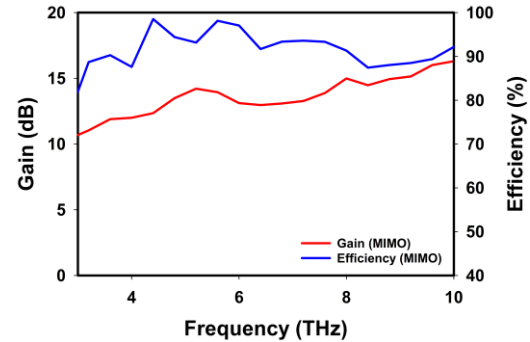


Fig. 10. Gain and efficiency curve of the proposed MIMO antenna.

### C. ECC and DG

In Fig. 11, we can observe the Envelope Correlation Coefficient (ECC) and Diversity Gain (DG) displayed as a frequency function simulated in THz. The Envelope Correlation Coefficient (ECC) is near zero (0.0001). A near-zero ECC indicates that the signals from different antenna elements are largely uncorrelated, which enhances the system's ability to exploit spatial diversity and improve signal quality [24]. ECC is calculated by the formula:

$$ECC = \frac{|\int_{4\pi} [E_1(\theta, \varphi) \times E_2(\theta, \varphi)] d\Omega|^2}{\int_{4\pi} |E_1(\theta, \varphi)|^2 d\Omega \int_{4\pi} |E_2(\theta, \varphi)|^2 d\Omega} \quad (1)$$

The Diversity Gain (DG) of the proposed antenna is 9.999 dB. The high diversity gain further confirms the antenna's capability to provide robust MIMO performance,

which is essential for modern high-speed communication systems [25]. DG can be calculated by the equation:

$$DG = 10\sqrt{1 - ECC^2} \quad (2)$$

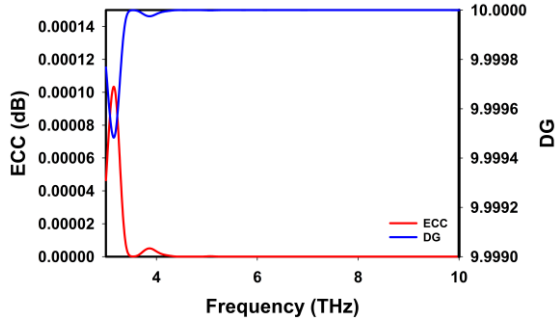


Fig. 11. The ECC and DG of the proposed antenna.

#### D. Radiation Pattern

We carefully analyzed the polar plot labeled as Fig. 12, which depicted the far-field electric field (E-field) at a 1-meter radius, specifically at an azimuth angle (Phi) of 90 degrees for our designed THz patch antenna [26]. The circular plot was marked with degrees from 0 to 360 around the circumference and radial lines at various angles, enabling precise data interpretation. Additionally, Fig. 12 presented important metrics, including a main lobe magnitude of  $-1.75$  dBV/m, a main lobe direction at  $70.0$  degrees, an angular width (3 dB) of  $31.9$  degrees, and a side lobe level at  $-1.7$  dB. The plot was meticulously annotated with Phi values at the circumference (Phi = 0, Phi = 90, Phi = 180, Phi = 270) to indicate angles in degrees, while the radial axis denoted the E-field strength in dBV/m. The bottom of the plot featured labeled axes, noting Theta (in degrees) versus E-field strength (dBV/m). The legend in the top right corner precisely identified the red line, representing the far-field broadband E-field data [27].

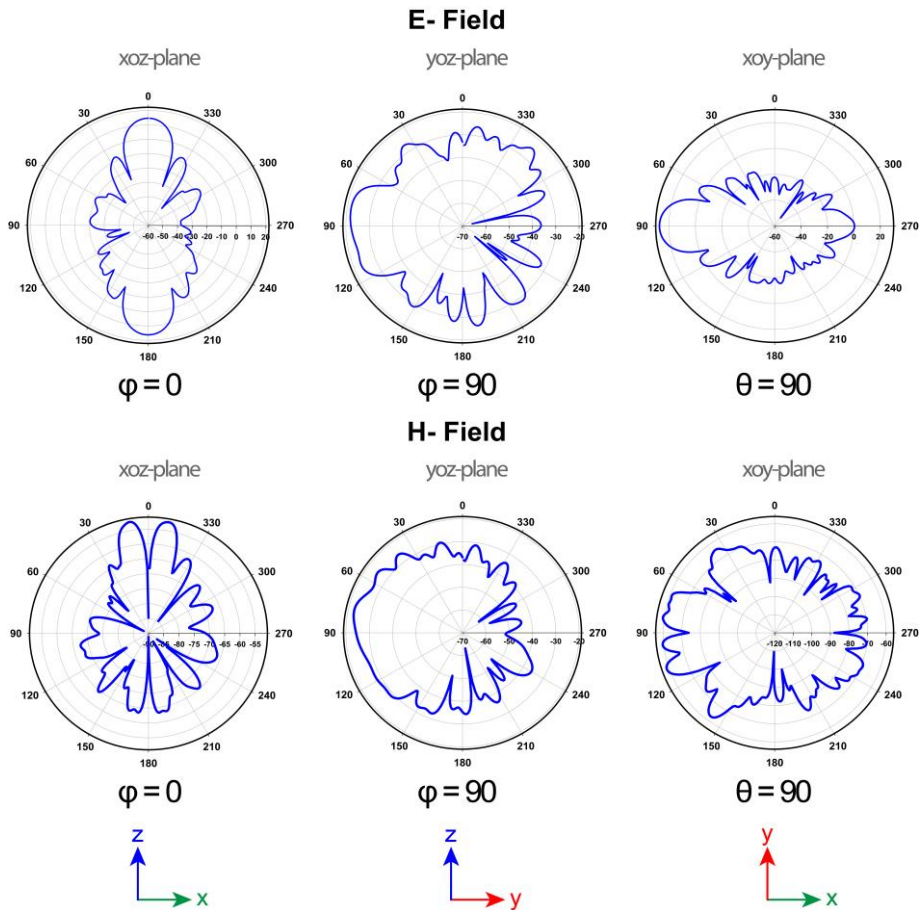


Fig. 12. Radiation pattern of the proposed MIMO antenna.

#### VII. RLC EQUIVALENT CIRCUIT AND RESULT ANALYSIS

The RLC equivalent circuit for our THz MIMO antenna design is comprised of several Resistors (R), Inductors (L), and capacitors (C) arranged in a specific topology. This configuration results in six distinct resonance frequencies: 3.5, 4.44, 6.7, 7.67, 8.66, and 9.67 THz. The resistors in the circuit are as follows:  $R1 = 45.79 \Omega$ ,  $R2 = 49.78 \Omega$ ,  $R3$

$= 57.27 \Omega$ ,  $R4 = 52.35 \Omega$ , and  $R5 = 50 \Omega$ , which are crucial in defining the damping factors and bandwidths of the resonant frequencies. The inductors in the circuit include:  $L1 = 0.0012$  H,  $L2 = 0.007$  H,  $L3 = 4.71$  H,  $L4 = 0.0029$  H,  $L5 = 7.34$  H,  $L6 = 0.12$ ,  $L7 = 0.12$  H,  $L8 = 1.37$  H and  $LX = 1.24$  H. These inductors play a vital role in the storage of magnetic energy and significantly influence the

oscillatory behavior of the circuit. The capacitors in the circuit are as follows:  $C1=0.0029$  F,  $C2=0.0072$  F,  $C3=4.71$  F,  $C4=5.32$  F,  $C5=2.78$  F,  $C6=0.79$  F,  $C7=6.38$  F,  $C8=1.43$  F, and  $CX=3.79$  F. These capacitors store electric energy and have a significant impact on the resonant frequencies and the overall impedance of the circuit. In Fig. 13 we can see the arrangement of these components in a complex network, where combinations of inductors and capacitors form resonant LC circuits, each corresponding to one of the resonance frequencies observed in the THz MIMO antenna and Fig. 14 shows the result of our CST and RLC circuit. This intricate design ensures the antenna operates efficiently across multiple frequencies, making it suitable for high-frequency applications in the terahertz range [28].

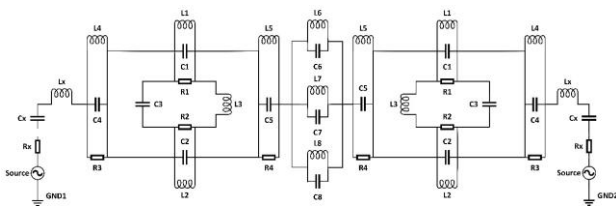


Fig. 13. RLC equivalent circuit of the proposed MIMO antenna.

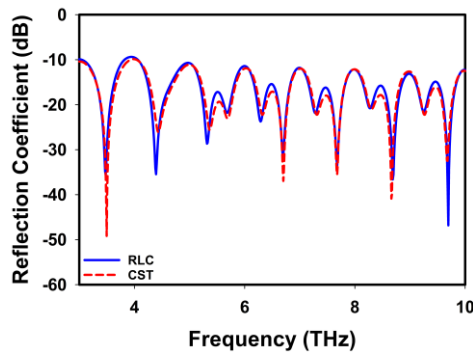


Fig. 14. ADS vs CST S11 of the proposed antenna.

### VIII. MACHINE LEARNING (ML) BASED OPTIMIZATION

When Comparing Electromagnetic (EM) software to Machine Learning (ML), it is evident that ML offers significant advancements in antenna design, primarily due to its reduced computational time [29]. Traditional electromagnetic solvers, such as Finite Element Methods (FEM) and Finite Difference Time Domain (FDTD), can take hours or even days to complete simulations. In contrast, machine learning algorithms can quickly predict antenna performance after training, facilitating iterative design improvements [30]. This speed can be beneficial for industries that operate at a rapid pace, including IoT, aerospace, and telecommunications [31]. ML has several key benefits compared to conventional EM programs:

#### A. Enhanced Productivity in the Design Process

Traditional methods often require tedious manual adjustments and repetitive simulations, which may not always yield optimal results. Machine learning accelerates

this process by automatically seeking the best solutions across extensive design spaces.

#### B. Front-End Performance Prediction

Engineers can leverage ML models to evaluate antenna performance early in the design phase. The model can automatically generate designs that meet specified criteria, contrasting sharply with the iterative modifications and ongoing result analysis typically demanded by traditional EM solvers.

#### C. Increased Robustness against Real-World Disruptions

While classical EM solvers function under idealized conditions, ML models can account for the environmental variations, fabrication tolerances, and material property changes that occur during actual manufacturing processes.

#### D. Simultaneous Optimization of Multiple Objectives

ML facilitates the optimization of various design parameters at once, leading to more comprehensive solutions. In contrast, traditional EM solvers often rely on a one- or two-parameter approach, necessitating numerous simulation cycles for design refinement.

#### E. Preparing Data Sets

This diagram in Fig. 15 illustrates how a machine learning model functions in the context of antenna design by depicting the relationship between its input parameters and output. Key factors such as ground width, feed length (at 50 ohms), substrate and patch thickness, as well as substrate length and width, serve as the inputs for the model. The machine learning algorithm processes these variables to predict the antenna's resonance frequency. In the realm of optimizing antenna design, the model's ability to assess these input parameters and accurately generate the resonance frequency represents a promising technique.

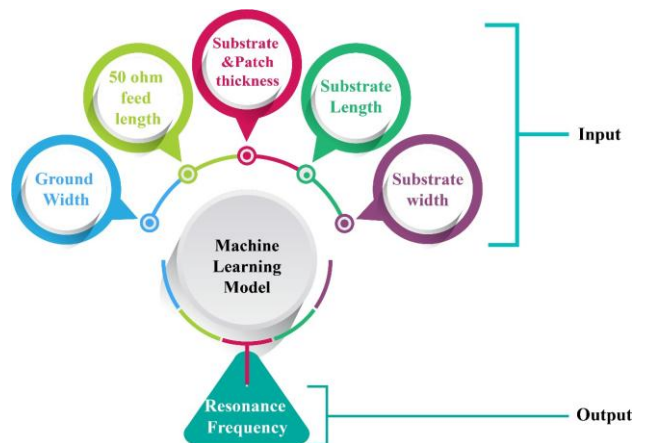


Fig. 15. ML model for the proposed work.

The flowchart illustrates the process of predicting antenna performance using Machine Learning (ML) algorithms. The first step involves antenna design and the generation of datasets through parameter variation. Next, the dataset is divided, with 80% allocated for training and 20% reserved for testing as depicted in Fig. 16 [32]. During the training phase, several ML methods are

employed, including Non-Parametric Regression, Gradient Boosting, Random Forests, XGBoost, and Extra Trees. The accuracy of the trained model is then evaluated using the testing data. Finally, the most accurate model is selected to predict the antenna's resonance frequency or other properties by choosing the algorithm that demonstrates the best performance.

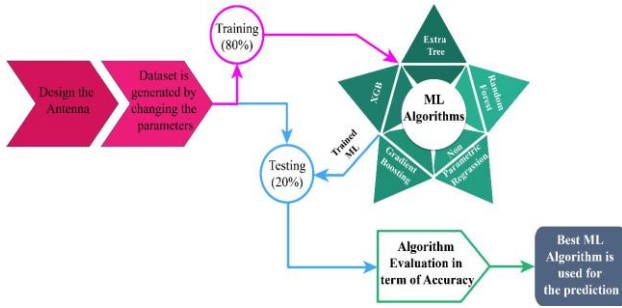


Fig. 16. The flowchart of the ML for the proposed work.

### F. Selection of Algorithm

The choice of a Machine Learning (ML) algorithm for antenna design is contingent upon aspects like data complexity, accuracy, interpretability, speed, and generalization. Tree-based algorithms such as Random Forests or XGBoost are optimal for huge, complicated datasets with intricate linkages, as they effectively manage high-dimensional data and discern detailed patterns. Random Forests, XGBoost, and Extra Trees are favored for their accuracy and resilience to overfitting, particularly in the presence of noisy data. If interpretability is paramount, one could opt for simpler models such as Non-Parametric Regression or Gradient Boosting. For faster computation and real-time design adjustments, algorithms like Random Forests or Extra Trees are efficient, while Gradient Boosting and XGBoost excel in generalization.

#### 1) Gradient boost regression

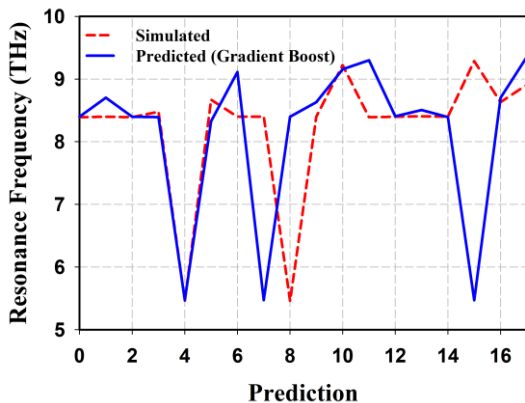


Fig. 17. Simulated vs predicted resonant frequency for gradient boost regression.

Gradient Boosting Regression builds decision trees sequentially to enhance predictive accuracy. Each new tree addresses the errors of previous trees, thereby improving performance. By calculating the residuals from earlier forecasts, new models are trained to predict and reduce

these errors [33]. The graph illustrates a comparison between the simulated resonance frequency (represented by the red dashed line) and the anticipated resonance frequency (indicated by the blue solid line) at various prediction points of the Gradient Boost Regression model. The y-axis represents the resonance frequency in terahertz, while the x-axis displays the prediction index. Both the simulated and projected frequencies exhibit considerable fluctuations. However, there is a significant divergence between the two lines, suggesting that the prediction model may not accurately replicate the simulated data as shown in Fig. 17.

#### 2) Non-parametric regression

Non-parametric regression, a form of regression analysis, does not require assumptions about the underlying data distribution or the functional relationship between variables [34]. Two prominent examples of non-parametric approaches are decision trees and K-Nearest Neighbors (KNN), both of which provide greater flexibility in capturing complex, non-linear patterns in data compared to parametric models that rely on a predefined structure. This method is especially useful when the relationship between the target variable and the predictors is intricate or uncertain, making traditional parametric models unsuitable. For non-parametric regression model, the graphic compares simulated and predicted resonance frequency values over different prediction points. Simulation data is the red dashed line, while anticipated values are the blue solid line as depicted in Fig. 18. The graph shows how well the predicted resonance frequency matches the simulated one, with some minor changes, demonstrating the model's performance and ability to approximate true values. The x-axis shows prediction points and the y-axis THz resonance frequency.

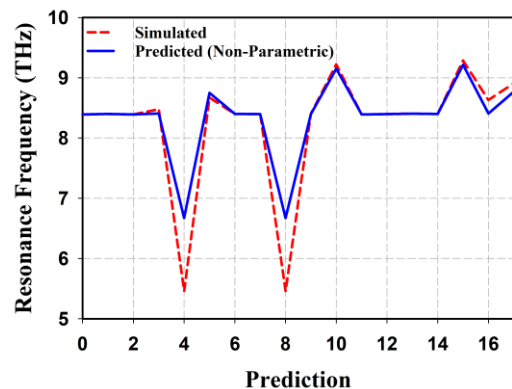


Fig. 18. Simulated vs predicted resonant frequency for non-parametric regression.

#### 3) Random forest regression

Random Forest Regression utilizes multiple decision trees to make predictions. It averages the predictions from each tree, which is trained on a random subset of the data, to arrive at the result. This diversity among the trees helps to reduce overfitting and enhance accuracy. Random Forest Regression is particularly effective for regression tasks involving non-linear patterns and high-dimensional

characteristics, as it excels at capturing complex relationships within the data [35]. The graphic compares simulated (red dashed line) and anticipated (blue solid line) resonance frequencies across prediction sites. As with the previous graph, the prediction model deviates slightly from the simulated data around peaks. The random forest regression model’s resonant frequency predictions are comparatively better to the simulated values, indicating improving approximation as illustrated in Fig. 19. Prediction points are on the x-axis, and THz resonance frequency is on the y-axis.

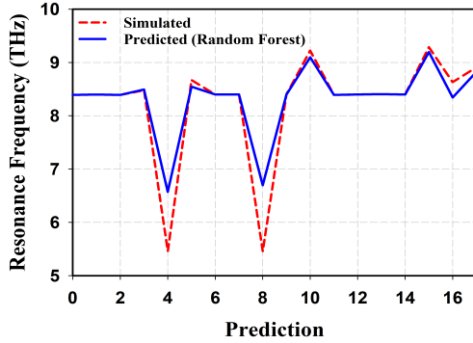


Fig. 19. Simulated vs predicted resonant frequency for random forest regression.

4) XGBoost regression

XGBoost Regression is a robust and effective machine-learning approach that employs gradient-boosting methods for predictive analysis. XGBoost, an acronym for “Extreme Gradient Boosting,” constructs a sequence of decision trees, with each tree rectifying the flaws of its predecessor. It is recognized for its rapidity and precision, employing regularization methods to avert overfitting. XGBoost is especially proficient for extensive datasets and intricate regression tasks, establishing it as a premier option for predictive modeling in data science competitions [36]. The plot contrasts simulated (red dashed line) and anticipated (blue solid line) resonance frequency values, as in prior graphs. With just slight differences, the XGBoost regression model predicts the simulated data as plotted in Fig. 20.

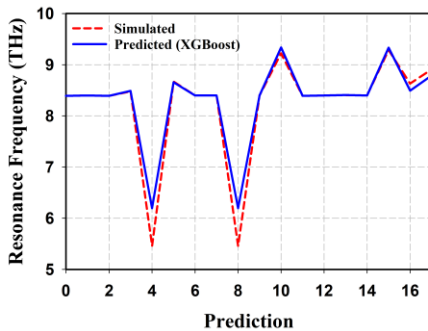


Fig. 20. Simulated vs predicted resonant frequency for XGBoost regression.

5) Extra trees regression

Extra Trees Regression, an ensemble learning method, constructs extra decision trees using random splits at each

node instead of the optimal split. Increased randomization reduces overfitting and enhances generalization. Extra Trees is fast, efficient, and performs well in high-dimensional datasets for difficult regression applications [37]. The Extra Trees regression model fits the simulated resonance frequency values well (red dashed line) and predicted resonance frequency values (blue solid line). Most predictions match simulated values, with barely noticeable differences as depicted in Fig. 21. This suggests that the Extra Trees model accurately collects data patterns and approximates resonance frequency.

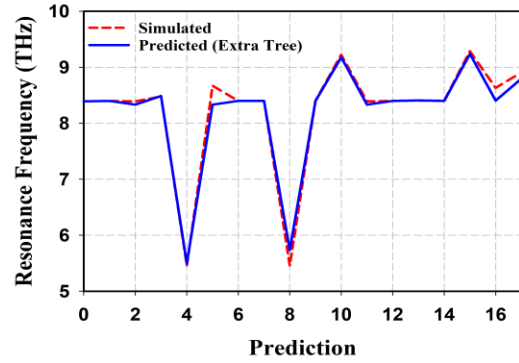


Fig. 21. Simulated vs predicted resonant frequency for extra tree regression.

G. Performance Evaluation Criteria for Regression Models

TABLE III. OVERVIEW OF ASSESSMENT MEASURES FOR REGRESSION ANALYSIS

Metric	Equation
Mean Absolute Error (MAE)	$\frac{1}{n} \sum_{i=1}^n  y_i - \hat{y}_i $
Mean Squared Error (MSE)	$\frac{1}{n} \sum_{i=1}^n (y_i - \hat{y}_i)^2$
Root Mean Squared Error (RMSE)	$\sqrt{\frac{1}{n} \sum_{i=1}^n (y_i - \hat{y}_i)^2}$
R-square	$1 - \frac{\sum_{i=1}^N (y_i - \hat{y}_i)^2}{\sum_{i=1}^N (y_i - \bar{y})^2}$
variance score	$1 - \frac{\text{Var}(y - \hat{y})}{\text{Var}(y)}$

To assess regression models, it’s essential to utilize metrics that indicate the accuracy of the results. Common metrics include Mean Absolute Error (MAE), which calculates the average absolute difference between predicted and actual values and Mean Squared Error (MSE) and Root Mean Squared Error (RMSE), which place greater emphasis on larger errors [38]. RMSE is particularly useful as it provides value in the same units as the target variable, facilitating easier interpretation. Additionally, the Variation Score measures the extent to which the model accounts for the variation in the target variable, while R-squared evaluates how effectively the model explains the variance within the target variable. The

equations of the performance metrics is illustrated in Table III [39].

H. Analysis of Regression Machine Learning Based Prediction Results:

Table IV presents the effectiveness of various machine learning techniques in predicting resonance frequency. It includes metrics such as MAE (Mean Absolute Error), MSE (Mean Squared Error), RMSE (Root Mean Squared Error), R<sup>2</sup> (Coefficient of Determination), and EVS (Explained Variance Score). The findings indicate that Extra Trees Regression outperforms the others, as evidenced by its lowest MAE, MSE, and RMSE values, along with the highest R<sup>2</sup> and EVS scores. XGBoost Regression also demonstrates strong performance. In contrast, Gradient Boost Regression and Non-Parametric Regression show comparatively weaker results. These results suggest that ensemble models like Extra Trees and XGBoost can be more effective for this predictive task.

TABLE IV. PERFORMANCE COMPARISON OF VARIOUS REGRESSION MODELS

The Resonance Frequency Prediction Performance					
Algorithm	MAE	MSE	RMSE	R <sup>2</sup>	EVS
Gradient Boost Regression	21.17%	46.62%	68.28%	75.30%	77.09%
Non-Parametric Regression	17.15%	16.80%	40.99%	83.75%	84.84%
Random Forest Regression	17.12%	16.09%	40.12%	85.24%	86.12%
XGBoost Regression	10.64%	6.28%	25.06%	93.92%	94.47%
Extra Trees Regression	6.69%	1.47%	12.14%	98.57%	98.67%

The graph presents the error metrics (MAE, MSE, RMSE) for various regression techniques. Extra Trees Regression demonstrates the lowest error metrics, achieving a Mean Absolute Error (MAE) of 6.69%, a Mean Squared Error (MSE) of 1.47%, and a Root Mean Squared Error (RMSE) of 12.14% as shown in Fig. 22. In comparison, XGBoost Regression records a Mean Absolute Error (MAE) of 10.64%, a Mean Squared Error (MSE) of 6.28%, and a Root Mean Squared Error (RMSE) of 25.06%. Random Forest Regression follows with a Mean Absolute Error (MAE) of 17.12%, a Mean Squared Error (MSE) of 16.09%, and a Root Mean Squared Error (RMSE) of 40.12%. Non-Parametric Regression shows a slight edge over Gradient Boost Regression, with an MAE of 17.15%, an MSE of 16.80%, and an RMSE of 40.99%. Gradient Boost Regression has the highest error metrics, reporting a Mean Absolute Error (MAE) of 21.17%, a Mean Squared Error (MSE) of 46.62%, and a Root Mean Squared Error (RMSE) of 68.28%. These results highlight Extra Trees as the most effective models, given their lower error metrics.

The graph presents a comparison of the R<sup>2</sup> and VAR scores across various regression techniques. Extra Trees Regression demonstrates exceptional performance, achieving an R<sup>2</sup> of 98.57% and a VAR Score of 98.67% as illustrated in Fig. 23. XGBoost Regression follows with

an R<sup>2</sup> of 93.92% and a VAR Score of 94.47%. Random Forest Regression records an R<sup>2</sup> of 85.24% and a VAR Score of 86.12%, while Non-Parametric Regression reaches an R<sup>2</sup> of 83.75% and a VAR Score of 84.84%. Gradient Boost Regression, on the other hand, shows the weakest performance, with an R<sup>2</sup> of 75.30% and a VAR Score of 77.09%. These results indicate that Extra Tree regression is the most accurate model for predicting resonance frequency.

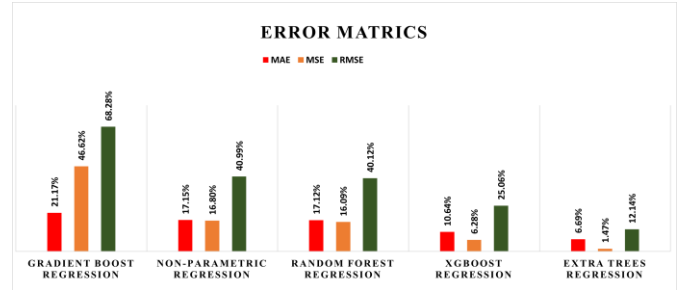


Fig. 22. Performance error metric bar chart.

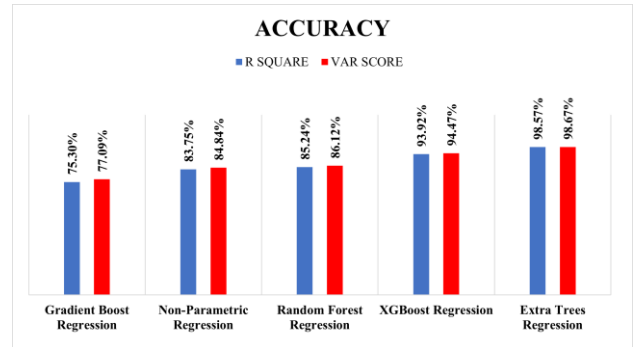


Fig. 23. Performance accuracy bar chart.

IX. PRACTICAL FEASIBILITY AND INTEGRATION CONSIDERATIONS

Beyond its promising electromagnetic characteristics, the proposed antenna demonstrates favorable attributes for real-world implementation. The selection of graphene and polyimide enables compatibility with advanced fabrication technologies such as photolithography and inkjet printing, which are capable of achieving the required dimensional precision at terahertz frequencies. These materials are also known for their mechanical flexibility, chemical stability, and scalability, making them suitable for integration into modern fabrication workflows. In terms of thermal performance, polyimide substrates can endure processing temperatures exceeding 300°C [40], while graphene retains high carrier mobility and conductivity under thermal stress, ensuring robust performance in heat-sensitive THz systems [41]. Furthermore, the compact, planar geometry of the antenna makes it well-suited for integration into 6G transceiver systems, including chip-level and package-level platforms, where multiband operation, high gain, and strong isolation are essential. These factors collectively support the practical viability of the proposed antenna in emerging 6G communication technologies.

## X. CONCLUSION

The THz MIMO antenna design demonstrates exceptional performance across six resonance frequencies, indicating strong potential for high-speed, high-frequency applications. Furthermore, the high isolation between ports, significant gain, and efficiency values underscores the antenna's superior performance. The near-zero ECC and high DG values validate the antenna's ability to deliver robust MIMO performance, a critical feature for modern communication systems. Moreover, the RLC circuit model for the S11 parameter provides valuable insights into the antenna's electrical behavior, enabling further optimization and application-specific adjustments. Moreover, the antenna demonstrates remarkably low error rates in predicting resonant frequencies, exhibiting a Mean Absolute Error (MAE) of 6.69%, a mean squared error (MSE) of 1.47%, and a root mean squared error (RMSE) of 12.14%. These results highlight its exceptional performance for future 6G applications, as validated through resonant frequency calculations and projections utilizing Extra Tree Regression. Future research can investigate reconfigurable designs for dynamic frequency adaptability, the effects of graphene properties under varying conditions, and miniaturization for wider applications, including IoT and satellite communication. These advancements can help propel terahertz technology and next-generation communication systems.

## CONFLICT OF INTEREST

The authors declare no conflict of interest.

## AUTHOR CONTRIBUTIONS

Ashraful Haque: Conceptualization, Methodology, Formal analysis, and Software; Sharif Ahammed: Conceptualization, Methodology, Writing – Original Draft, and Writing – Review & Editing; Jun-Jiat Tiang: Formal analysis, Project administration, and Validation; Narinderjit Singh Sawaran Singh: Resources, Supervision; Jamal Hossain Nirob: Supervision, Validation, Writing - Review & Editing; all authors had approved the final version.

## ACKNOWLEDGMENT

The authors extend their appreciation to acknowledge the Information and Communication Technology Division (ICTD), Agargaon, Dhaka, Bangladesh, for funding this research work through grant number No: 56.00.0000.000.052.33.0003.24-130.

## REFERENCES

- [1] M. Banafaa *et al.*, "6G mobile communication technology: Requirements, targets, applications, challenges, advantages, and opportunities," *Alexandria Engineering Journal*, vol. 64, pp. 245–274, Feb. 2023.
- [2] G. Saxena, Y. K. Awasthi, and P. Jain, "High isolation and high gain super-wideband (0.33–10 THz) MIMO antenna for THz applications," *Optik*, vol. 223, 165335, Dec. 2020.
- [3] S. A. Khaleel, E. K. I. Hamad, and M. B. Saleh, "High-performance tri-band graphene plasmonic microstrip patch antenna using superstrate double-face metamaterial for THz communications," *Journal of Electrical Engineering*, vol. 73, no. 4, pp. 226–236, Aug. 2022.
- [4] T. Okan, "High efficiency unslotted ultra-wideband microstrip antenna for sub-terahertz short range wireless communication systems," *Optik*, vol. 242, 166859, Sep. 2021.
- [5] M. A. Haque *et al.*, "Performance improvement of THz MIMO antenna with graphene and prediction bandwidth through machine learning analysis for 6G application.," *Results in Engineering*, 103216, Oct. 2024.
- [6] S. Fakhte and M. M. Taskhiri, "Graphene-based terahertz antenna with polarization reconfiguration," *Phys. Scr.*, vol. 98, no. 11, 115541, Nov. 2023.
- [7] R. Pant and L. Malviya, "THz antennas design, developments, challenges, and applications: A review," *Int. J. Communication*, vol. 36, no. 8, e5474, May 2023.
- [8] K. Ahmed *et al.*, "Graphene-based THz antenna with a wide bandwidth for future 6G short-range communication," *Telkomnika*, vol. 23, no. 2, p. 306, Apr. 2025.
- [9] S. A. Khaleel, E. K. I. Hamad, N. O. Parchin, and M. B. Saleh, "MTM-Inspired graphene-based THz MIMO antenna configurations using characteristic mode analysis for 6G/IoT applications," *Electronics*, vol. 11, no. 14, 2152, Jul. 2022.
- [10] S. A. Khaleel, E. K. I. Hamad, N. O. Parchin, and M. B. Saleh, "Programmable beam-steering capabilities based on graphene plasmonic THz MIMO antenna via Reconfigurable Intelligent Surfaces (RIS) for IoT applications," *Electronics*, vol. 12, no. 1, p. 164, Dec. 2022.
- [11] N. S. Asaad, A. M. Saleh, and M. A. Alzubaidy, "Analyzing performance of THz band graphene-based MIMO antenna for 6G applications," *Journal of Telecommunications and Information Technology*, vol. 3, pp. 23–29, 2024.
- [12] A. A. Ibrahim and S. M. Gaber, "Frequency reconfigurable antipodal vivaldi 2-port antenna based on graphene for terahertz communications," *Opt. Quant. Electron*, vol. 55, no. 9, p. 786, Sep. 2023.
- [13] Y. Amraoui, I. Halkhams, R. E. Alami, M. O. Jamil, and H. Qjidaa, "High isolation integrated four-port MIMO Antenna for terahertz communication," *Results in Engineering*, vol. 26, 105253, Jun. 2025.
- [14] A. Kumar, D. Saxena, P. Jha, and N. Sharma, "Compact two-port antenna with high isolation based on the defected ground for THz communication," *Results in Optics*, vol. 13, 100522, Dec. 2023.
- [15] K. V. Babu, S. Das, G. N. J. Sree, B. T. P. Madhav, S. K. K. Patel, and J. Parmar, "Design and optimization of micro-sized wideband fractal MIMO antenna based on characteristic analysis of graphene for terahertz applications," *Opt. Quant. Electron*, vol. 54, no. 5, p. 281, May 2022.
- [16] Y. Amraoui, I. Halkhams, R. E. Alami, M. O. Jamil, and H. Qjidaa, "High gain MIMO antenna with multiband characterization for terahertz applications," *Scientific African*, vol. 26, e02380, Dec. 2024.
- [17] K. Herath, A. Nirmalathas, S. D. Gunapala, and M. Premaratne, "Floquet engineering-based frequency demodulation method for wireless THz short-range communications," *Phys. Scr.*, vol. 98, no. 9, 095021, Sep. 2023.
- [18] A. Haque *et al.*, "High-bandwidth millimetre wave multiple-input multiple-output antenna for 38 GHz 5G mobile applications," *TELKOMNIKA*, vol. 23, no. 2, p. 283, Apr. 2025.
- [19] J. H. Nirob *et al.*, "Dual-band MIMO antenna for wideband THz communication in future 6G applications," *TELKOMNIKA*, vol. 23, no. 2, p. 295, Apr. 2025.
- [20] K. V. Babu, S. Das, G. Varshney, G. N. J. Sree, and B. T. P. Madhav, "A micro-scaled graphene-based tree-shaped wideband printed MIMO antenna for terahertz applications," *Journal of Computational Electronics*, vol. 21, no. 1, pp. 289–303, Feb. 2022.
- [21] M. F. Ali, R. Bhattacharya, and G. Varshney, "Tunable four-port MIMO/self-multiplexing THz graphene patch antenna with high isolation," *Opt. Quant Electron*, vol. 54, no. 12, p. 822, Dec. 2022.
- [22] N. Rashid, L. C. Paul, T. Rani, A. Majumder, M. A. Haque, and M. Karaaslan, "A compact wideband CPW-fed modified semi-vivaldi antenna for Ku-band applications," in *Proc. 2022 25th International Conference on Computer and Information Technology (ICCIT)*, 2022, pp. 1098–1103.
- [23] A. D'Arco *et al.*, "Terahertz continuous wave spectroscopy: A portable advanced method for atmospheric gas sensing," *Opt. Express*, vol. 30, no. 11, 19005, May 2022.

- [24] R. Pant and L. Malviya, "Terahertz MIMO antenna array for future generation of wireless applications," *Frequenz*, Feb. 2024. doi: 10.1515/freq-2023-0203
- [25] H.-J. Song and T. Nagatsuma, "Present and future of Terahertz communications," *IEEE Trans. Terahertz Sci. Technol.*, vol. 1, no. 1, pp. 256–263, Sep. 2011.
- [26] A. Rahman, S. S. Al-Bawri, M. T. Islam, M. J. Singh, D. Saha, and Md. A. Haque, "A compact multiband microstrip antenna design for 5G IoT and satellite communication applications," in *Proc. 8th International Conference on Space Science and Communication*, 2024, pp. 125–132.
- [27] P. Das, "Beam-steering of THz MIMO antenna using graphene-based intelligent reflective surface," *Opt. Quant Electron*, vol. 55, no. 8, p. 711, Aug. 2023.
- [28] J. H. Nirob *et al.*, "Optimized tri-band MIMO antenna design for 6G terahertz applications and future connectivity," *TELKOMNIKA*, vol. 23, no. 2, p. 553, 2025.
- [29] A. Haque *et al.*, "Machine learning-based technique for directivity prediction of a compact and highly efficient 4-Port MIMO antenna for 5G millimeter wave applications," *Results in Engineering*, 103106, Oct. 2024.
- [30] A. Haque *et al.*, "Broadband high gain performance MIMO antenna array for 5 G mm-wave applications-based gain prediction using machine learning approach," *Alexandria Engineering Journal*, vol. 104, pp. 665–679, Oct. 2024.
- [31] K. Ahmed *et al.*, "based performance estimation of a slotted inverted F-shaped tri-band antenna for satellite/mm-wave 5G application," *Telkommnika*, vol. 22, no. 4, p. 773, Aug. 2024.
- [32] A. Haque *et al.*, "Multiband THz MIMO antenna with regression machine learning techniques for isolation prediction in IoT applications," *Sci. Rep.*, vol. 15, no. 1, p. 7701, Mar. 2025.
- [33] A. Haque *et al.*, "Regression supervised model techniques THz MIMO antenna for 6G wireless communication and IoT application with isolation prediction," *Results in Engineering*, 103507, Nov. 2024.
- [34] A. Haque *et al.*, "Machine learning-based technique for gain prediction of mm-wave miniaturized 5G MIMO slotted antenna array with high isolation characteristics," *Sci. Rep.*, vol. 15, no. 1, p. 276, Jan. 2025.
- [35] S. S. A. Bawri *et al.*, "Machine learning technique based highly efficient slotted 4-port MIMO antenna using decoupling structure for sub-THz and THz 6G band applications," *Opt. Quant. Electron*, vol. 56, no. 10, p. 1611, Sep. 2024.
- [36] M. A. Haque *et al.*, "Machine learning based compact MIMO antenna array for 38 GHz millimeter wave application with robust Isolation and high efficiency performance," *Results in Engineering*, 104006, Jan. 2025.
- [37] M. A. Haque *et al.*, "Machine learning-based novel-shaped THz MIMO antenna with a slotted ground plane for future 6G applications," *Sci. Rep.*, vol. 14, no. 1, 32162, Dec. 2024.
- [38] N. S. S. Singh *et al.*, "Dual band antenna design for 4G/5G application and prediction of gain using machine learning approaches," *Telkommnika*, vol. 23, no. 2, p. 543, Apr. 2025.
- [39] K. H. Nahin *et al.*, "Performance prediction and optimization of a high-efficiency tessellated diamond fractal MIMO antenna for terahertz 6G communication using machine learning approaches," *Sci. Rep.*, vol. 15, no. 1, p. 4215, Feb. 2025.
- [40] P. Xiao, X. He, and Q. Lu, "Exceptionally high-temperature-resistant kapton-type polyimides with  $T_g > 520^\circ\text{C}$ : Synthesis via incorporation of Spirobis (indene)-bis(benzoxazole)-containing diamines," *Polymers*, vol. 17, no. 7, p. 832, Mar. 2025.
- [41] S. Lei, N. Su, and M. Li, "Thermal-resistance effect of graphene at high temperatures in nanoelectromechanical temperature sensors," *Micromachines*, vol. 13, no. 12, 2078, Nov. 2022.

Copyright © 2026 by the authors. This is an open access article distributed under the Creative Commons Attribution License which permits unrestricted use, distribution, and reproduction in any medium, provided the original work is properly cited ([CC BY 4.0](https://creativecommons.org/licenses/by/4.0/)).